

Effect of Process Atmosphere Dew Point and Tin Addition on Oxide Morphology and Growth for a Medium-Mn Third Generation Advanced Steel During Intercritical Annealing



MAEDEH POURMAJIDIAN, BRIAN LANGELIER, and JOSEPH R. MCDERMID

The combined effects of process atmosphere oxygen partial pressure, annealing time, and a 0.05 wt pct Sn addition on the selective oxidation of a model 0.1C-6Mn-2Si third generation advanced high-strength steel (3G-AHSS) composition were investigated. External and internal oxidation of both steels were observed after intercritical annealing at 963 K (690 °C) for holding times of 60 to 600 seconds under all process atmosphere dew points explored—*i.e.*, 223 K, 243 K, and 278 K (− 50 °C, − 30 °C, and + 5 °C). The external MnO morphology was changed from compact and continuous film-like nodules to a fine and discrete globular morphology, with thinner external oxides, for the Sn-added steel. Cross-sectional TEM analysis revealed that the Sn addition also resulted in significant refinement of the internal oxide network. Kinetic studies showed that both the external and internal oxidation followed a parabolic rate law, where the Sn addition to the steel chemistry resulted in lower external and internal oxidation rates. 3D atom probe tomography of the external oxide/steel interface showed that Sn was segregated to the interface with enrichment levels ten times the bulk value, which was concluded to be responsible for the observed morphological changes. The resultant refined external oxide structure is expected to have significant benefits with respect to reactive wetting by the continuous galvanizing bath.

<https://doi.org/10.1007/s11661-018-4855-1>

© The Minerals, Metals & Materials Society and ASM International 2018

I. INTRODUCTION

THE increasing demand for lighter, safer, and more fuel-efficient vehicles legislated by energy and environmental agencies has resulted in third generation advanced high-strength steels (3G-AHSS) receiving significant interest from leading auto steel researchers and OEMs as candidate materials for the manufacturing of reduced mass automotive structural components.^[1–5] In particular, the 3G-AHSSs are being designed to possess a superior combination of high strength and ductility *vs* the first generation AHSSs at a lower cost and a leaner chemistry compared to the highly alloyed second generation AHSS, *e.g.*, twinning induced plasticity (TWIP) and austenitic stainless steels.^[1–4]

However, the use of these next generation materials requires innovative solutions for maintaining the structural integrity of the vehicle against corrosion, particularly since the desired weight reduction is generally brought about by the use of thinner material cross-sections and more complex geometries for manufactured parts. Continuous hot-dip galvanizing is a widely practiced, cost-effective industrial process for this purpose, where a zinc alloy coating is applied to sheet products after being heat treated in a dew-point controlled, reducing N₂-H₂ atmosphere. However, the annealing atmospheres commonly used in industrial practice are not reducing with respect to the commonly used alloying elements such as Mn, Si, Cr, and Al and, as a result, selective oxidation of these elements can occur at the surface and subsurface of the steel, possibly rendering the sheet surface incompatible for reactive wetting by the continuous galvanizing Zn-Al-Fe bath. For example, it has been shown that the presence of an integral, relatively thick external oxide layer can prevent the essential reactive wetting reactions^[6–8] from taking place at the steel/zinc interface during immersion in the Zn(Al,Fe) bath, resulting in poor coating adhesion and unacceptable final product quality.

MAEDEH POURMAJIDIAN and JOSEPH R. MCDERMID are with the McMaster Steel Research Centre, McMaster University, 1280 Main Street West, Hamilton, ON L8S 4L7, Canada. Contact e-mail: mcdermid@mcmaster.ca BRIAN LANGELIER is with the Canadian Centre for Electron Microscopy, McMaster University, 1280 Main Street West, Hamilton, ON L8S 4M1, Canada.

Manuscript submitted February 1, 2018.

Article published online August 3, 2018

A variety of solutions have been proposed to address this issue, where several authors have suggested tailoring the process atmosphere conditions such that external selective oxidation of the alloying elements is either hindered or transferred from the surface to the subsurface. This can be achieved through different routes, such as increasing the oxygen partial pressure (pO_2) of the process atmosphere,^[9–14] increasing the hydrogen content of the gas mixture,^[15] or implementing a pre-oxidation treatment prior to annealing.^[16,17] More recently, the known effect of surface segregation of minor alloying additions such as Sn and Sb on retarding the rates of surface reactions such as carburization^[18] and selective oxidation of Si in electrical steels,^[19] was leveraged into the area of AHSS processing in the continuous galvanizing line (CGL) to resolve the issue of alloying element selective oxidation in low-alloy CMnSi TRIP steels.^[20–22] In particular, it was shown that minor additions of surface active elements such as Sn,^[20,21] Sb,^[20] or Bi^[22] within the ranges of 0.05 to 1 wt pct, could modify the morphology of the Si-rich surface oxides from film-like to island-like such that significant improvements in the quality of the galvanized coating were obtained. It was reported that segregation of these elements to the surface occupied the oxygen adsorption sites, thereby decreasing the oxygen permeability and potentially changing the surface oxide chemistry and morphology.^[20–24] It was also pointed out that the surface segregation also changed the interfacial energies, which contributed to the observed morphological changes.^[25,26] However, despite the beneficial effects on the selective oxidation of AHSSs alloyed with surface active elements, care must be taken when employing this approach as alloying additions in excess of 0.05 wt pct of elements such as S and Sn are known to have detrimental effects on the grain boundary cohesion and mechanical properties.^[25,27]

With the pending emergence of 3G-AHSSs in automotive structures, it is imperative that means be developed to allow for the metallic coating of this alloy class. Among the proposed candidate compositions for 3G-AHSSs, medium-Mn steels have emerged as credible candidates to fill the 3G-AHSS property space.^[5,28–31] However, limited work has been performed on the galvanizing of these alloys and, in particular, there is limited information available on the effect of surface active elements on the selective oxidation of medium-Mn steels and their potential to favorably change external oxide thickness, morphology, and distribution to facilitate reactive wetting by the Zn(Al,Fe) continuous galvanizing bath. Thus, the objective of the present contribution is to determine the combined effects of varying the oxygen partial pressure—through altering the N₂-5 vol pct H₂ process atmosphere dew point—and an alloying addition of 0.05 wt pct Sn on the selective

oxidation, oxide morphology, oxide surface distribution, and oxidation kinetics of a model Fe-0.1C-6Mn-2Si (wt pct) 3G-AHSS. The results of this study will also be interpreted within the context of previously established knowledge on the effect of these factors on the reactive wetting of steel surfaces by the Zn(Al,Fe) galvanizing bath.^[32–35]

The results of this work will contribute to subsequent studies on the subject of reactive wetting mechanisms of the medium-Mn 3G steels, which are expected to be significantly more difficult to reactively wet relative to the first generation AHSSs.

II. EXPERIMENTAL

Two grades of 0.1C-6Mn-2Si steel sheets, a reference alloy and a Sn-added grade, were received in the full-hard cold-rolled condition with an approximate thickness of 1.2 mm. The detailed chemical composition of the experimental steels is given in Table I. Samples for selective oxidation comprising 10 × 50 mm² coupons were cut from the as-received steel sheets using an abrasive water-jet such that the rolling direction was parallel to the longitudinal axis of the samples. The sample surfaces were polished using 4000 grit SiC paper prior to annealing in order to minimize the effects of surface roughness on the surface oxidation studies. All samples were cleaned with acetone immediately prior to annealing.

Selective oxidation heat treatments were carried out in a dew-point controlled N₂-5 vol pct H₂ process atmosphere in the McMaster Galvanizing Simulator (Iwatani-Surtec), operational details of which are well documented and can be found elsewhere.^[10] Three process atmospheres with dew points of 223 K, 243 K, and 278 K (− 50 °C, − 30 °C, and + 5 °C) were used to explore the effect of process atmosphere oxygen partial pressure on the selective oxidation of Mn and Si. A detailed summary of the experimental process atmospheres utilized in this study is presented in Table II, where the corresponding values of pH_2O/pH_2 for each dew point used and oxygen partial pressure (pO_2) at the peak intercritical annealing temperature (IAT) for each process atmosphere were derived using the FREED thermodynamic database.^[36] Throughout the subsequent text, references to process atmospheres and their corresponding samples will be made by the designated atmosphere name per Table II.

Figure 1 shows a schematic of the experimental annealing cycle, where samples were isothermally held at the IAT of 963 K (690 °C) for holding times within the range of 60 to 600 seconds (Table II). Following the isothermal hold, samples were rapidly cooled to 343 K (70 °C) at a rate of − 10 K/s *via* N₂ gas quenching. The

Table I. Chemical Composition of the Experimental Steels (Weight Percent)

Steel Name	C	Mn	Si	Al	Sn	P	S	Mn/Si
Reference	0.106	6.241	2.023	0.040	0.005	0.006	0.003	3.09
0.05 pct Sn	0.100	6.165	2.050	0.032	0.049	0.006	0.004	3.01

Table II. Experimental Specifications of the N₂-5 Vol Pct H₂ Process Atmospheres at 963 K (690 °C) Peak Annealing Temperature

Atmosphere Name	Dew Point (K)	pH ₂ O/pH ₂	pO ₂ (atm)	Holding Time (s)
- 50DP	223	0.00125	1.20×10^{-27}	60, 120, 180, 360, 600
- 30DP	243	0.00998	7.69×10^{-26}	60, 120, 180, 360, 600
+ 5DP	278	0.17111	2.26×10^{-23}	60, 120, 180, 360, 600

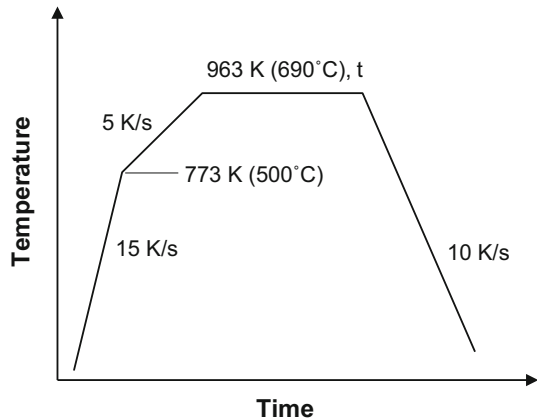


Fig. 1—Annealing heat treatment cycle schematic.

thermal cycle was controlled using a 0.5 mm type K thermocouple welded directly to one of the selective oxidation samples. All selective oxidation tests were carried out in triplicate to ensure repeatability of the experimental results. The heat-treated samples were stored in anhydrous HPLC grade isopropanol in order to minimize additional oxidation prior to analysis.

In order to study the effects of the experimental variables on surface oxide morphology and distribution, the annealed samples were examined in a JEOL 7000F field emission gun scanning electron microscope (FEG-SEM) operated in secondary electron imaging (SEI) mode at an acceleration voltage of 5 keV. All oxidized samples were coated with C prior to SEM analysis to prevent charging.

To investigate the formation and growth of the surface and subsurface oxides, SEM images were also acquired from the cross-sectioned surfaces revealed through focused ion beam (FIB) milling. A NVision 40 FIB-SEM microscope (Zeiss) equipped with an in-lens detector was operated at an acceleration voltage of 5 keV for electron imaging. Two trench cuts with a length of 10 μm each were made on distanced areas of all samples, prior to which C and W were deposited on those areas in order to preserve the surface oxides from damage during Ga ion beam milling. High-magnification electron images were captured along the length of the cuts where a tilt correction of 36 deg was applied to the cross-sectional images in order to compensate for the 54 deg stage tilt required for the milling procedure. Measurements of the external oxide layer thickness as well as the depth of the internal oxidation zone were performed using ImageJ 1.48v software. Oxide growth kinetics as a function of process atmosphere oxygen partial pressure and Sn addition were determined based

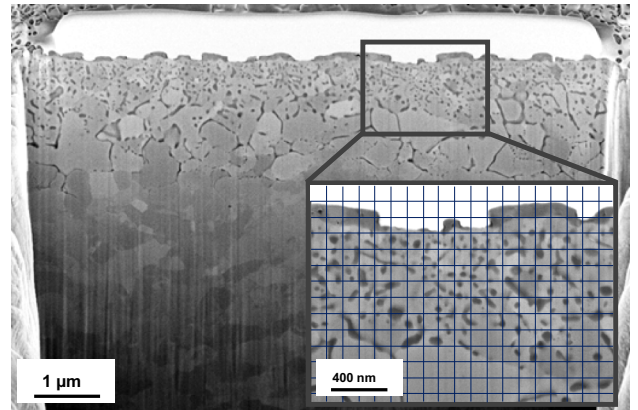


Fig. 2—Secondary electron-FIB images from the cross-section of the reference steel annealed under the + 5DP process atmosphere for 600 s; showing a 10-μm-trench cut and a higher magnification image with the sampling grid system superimposed for measurement purposes.

on a minimum of 100 measurements per sample taken using a defined sampling grid to ensure random sampling of the oxide layer thickness. An example of such an analysis along with a superimposed sampling grid is presented in Figure 2 to further illustrate this method. The average oxide thicknesses below are reported using the 95 pct confidence interval of the sample mean.

X-ray photoelectron spectroscopy (XPS) was carried out to identify the surface oxide chemistries and to obtain elemental depth profiles. The analysis was performed using a PHI Quantera SXM with an Al K_α X-ray source (1486.7 eV). The spot size was 100 μm and the take-off angle was set at 45 deg. Spectra were acquired using a pass energy of 140 eV and step size of 0.25 eV. Elemental depth profiles were obtained by Ar ion sputtering a 2 × 2 mm² area after sputtering the outermost 5 nm of the surface in order to remove contaminants arising from atmospheric exposure. Depth measurements are considered accurate within ± 10 pct of the documented sputtered depth. All data processing were performed using MultiPak 6.0 software. The reported binding energies are accurate to within ± 0.1 eV. All spectra were calibrated using the metallic Fe2p_{3/2} binding energy of 706.62 eV.

Scanning transmission electron microscopy (STEM) was performed on cross-sections of samples that were held for 600 seconds at the PAT across all process atmospheres explored. Similar to the procedure described above, FIB lift-outs were first made from areas of interest and were thinned by ion milling to meet the requirement for analysis with transmission electron microscopy. A FEI Titan 80-300HB transmission

electron microscope operated at 300 keV was used to acquire HR-STEM micrographs and to obtain electron energy loss spectra (EELS) using a Gatan Quantum GIF. Digital Micrograph 2.3 software was used to extract elemental maps from the raw EELS data.

In order to characterize Sn segregation to the surface and oxide/metal interfaces, 3D atom probe tomography (APT) was performed using a Cameca LEAP 4000X HR atom probe (Cameca Instruments). Prior to FIB lift-out, the sample surfaces were sputter-coated with a ~ 300-nm-thick layer of Cr to facilitate specimen preparation. FIB lift-outs containing the external oxide/metal interface and subsurface oxides were sectioned and mounted onto silicon posts using W deposition, and sharpened into needles by annular milling at 30 keV using standard methods.^[37] Final sharpening was done at 10 keV to remove FIB damage and position the external oxide/substrate interface at the tip apex. The tips were analyzed by APT operating in laser pulsing mode ($\lambda = 355$ nm, 60 pJ/pulse) with a stage temperature of ~ 60 K. The target detection rate was set at 0.005 ions/pulse (0.5 pct) which was maintained by an applied DC voltage. The laser pulsing rate was 120 or 200 kHz, as dictated by the applied voltage and maximum range of the mass spectrum. IVAS v3.6.6 software was used for reconstruction and analysis of the data.

III. RESULTS

A selection of SEM images of the external oxides formed during intercritical annealing at 963 K (690 °C) under the - 50DP, - 30DP, and + 5DP process

atmospheres are shown in Figures 3, 4, and 5, respectively, where the micrographs in (a), (b) and (c) represent the external oxides for the reference steel after 120-, 360-, and 600-second isothermal holds at the IAT and (d), (e), and (f) correspond to the same annealing parameters for the Sn-added grade. It should be recalled that five holding times within the range of 60 to 600 seconds were explored for the selective oxidation experiments; however, the trends shown in the present selection of SEM images were found to be consistent for all experimental samples.

It can be seen from Figure 3 that an increased coverage of the steel surface by the external oxides was observed with increasing annealing time. Furthermore, the oxide layers that were formed after the 360- and 600-second holds (Figures 3(b), (c), (e), and (f)) showed a coarser and more compact appearance. This coarsening trend with time was consistent for both of the reference and the Sn-added steels. However, a comparison of Figures 3(a) through (c) with their equivalent counterparts in Figures 3(d) through (f) clearly shows that the morphology and distribution of the oxides formed at the surface of the Sn-added grade were modified. For example, it can be seen that the Sn-added alloy external oxides comprised finer nodules with a globular morphology as opposed to the coarser, more compact, and film-like nodules of the reference alloy. It can also be observed that the Sn-added alloy surfaces exhibited a more discrete distribution with wider spacing between the nodules. Furthermore, it can be surmised that the surfaces of the Sn-added steel were significantly less oxidized, as exemplified most clearly in the case of the 120- and 360-second samples (*i.e.*, Figures 3(a) vs (d)

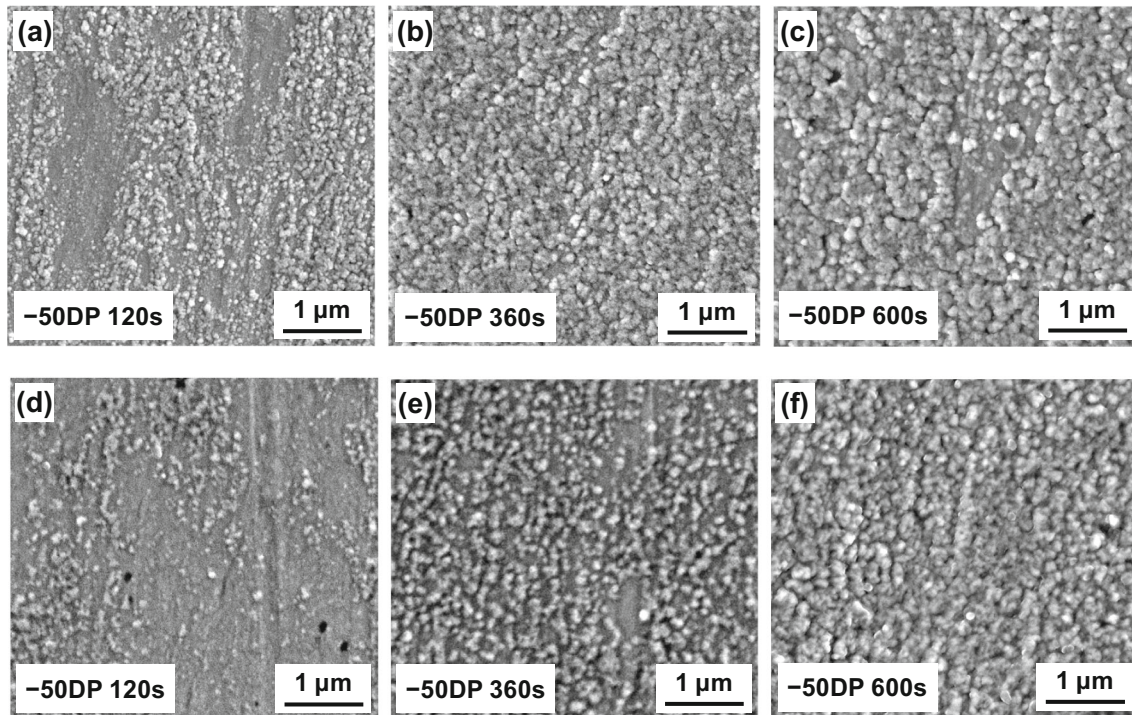


Fig. 3—Secondary electron images showing the surface oxide morphology of samples annealed under the - 50DP process atmospheres for 120, 360, and 600 s; (a) through (c) reference steel, (d) through (f) Sn-added steel.

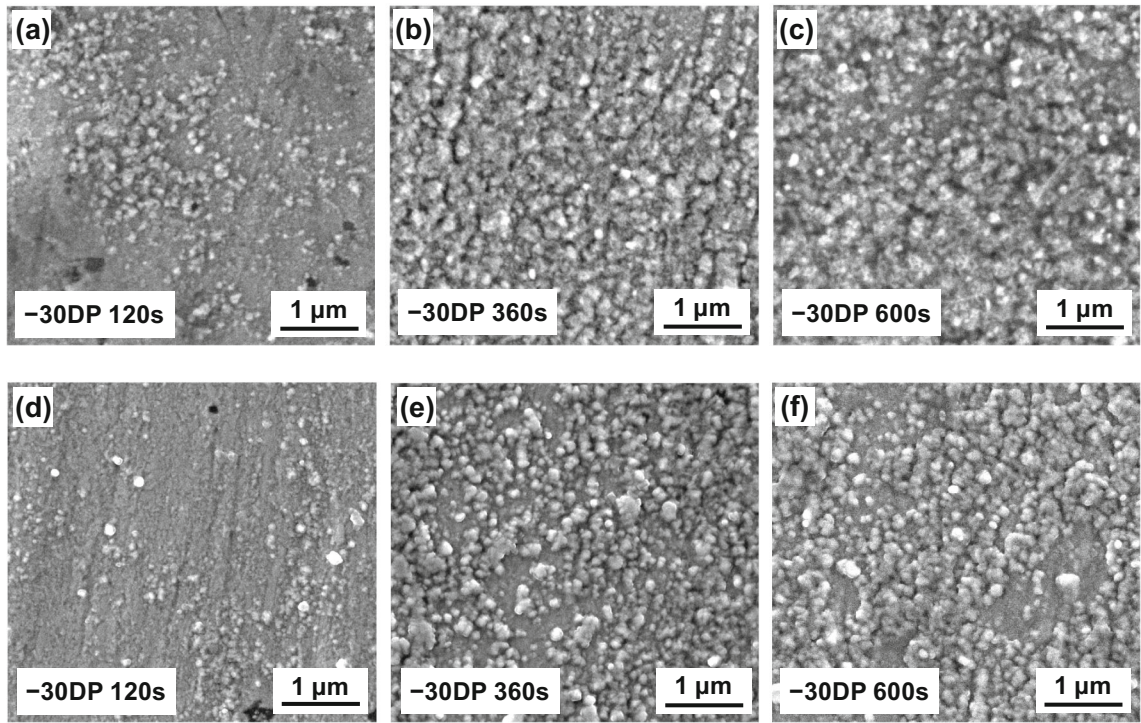


Fig. 4—Secondary electron images showing the surface oxide morphology of samples annealed under the – 30DP process atmospheres for 120, 360, and 600 s; (a) through (c) reference steel, (d) through (f) Sn-added steel.

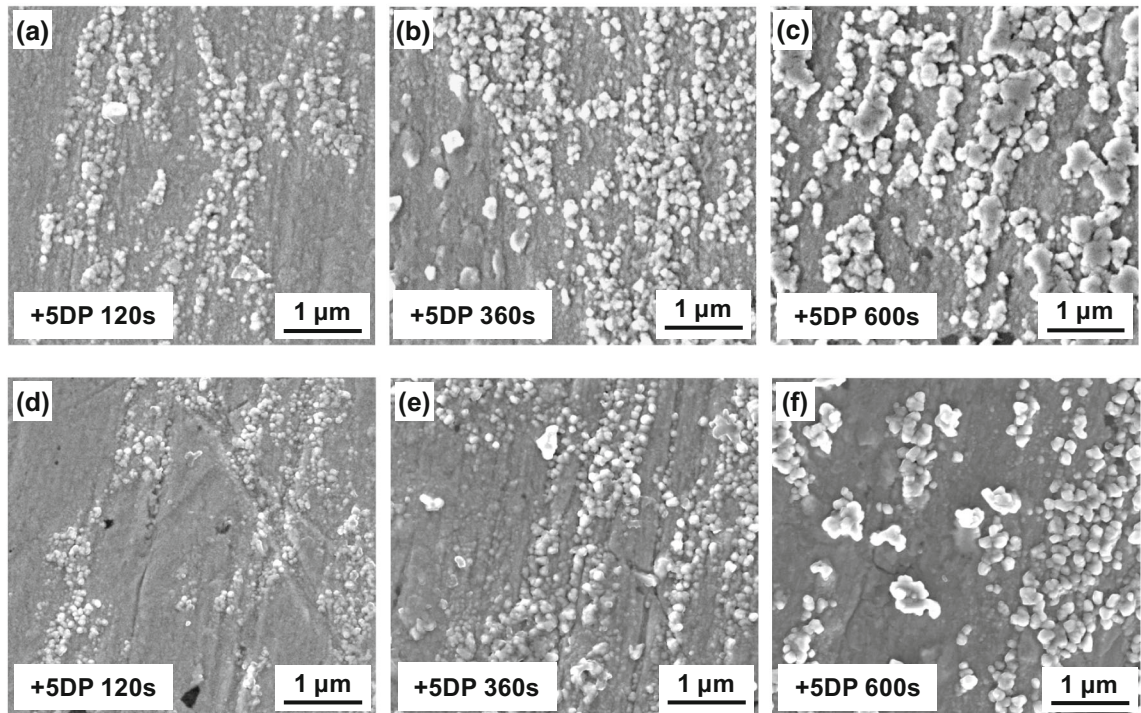


Fig. 5—Secondary electron images showing the surface oxide morphology of samples annealed under the + 5DP process atmospheres for 120, 360, and 600 s; (a) through (c) reference steel, (d) through (f) Sn-added steel.

and (b) vs (e)), whereas after the extended holding time of 600 seconds, a fully coarsened and compact external oxide scales were formed on both grades (*i.e.*, Figures 3(c) and (f)).

The modifying effect of the 0.05 wt pct Sn addition on the surface oxide morphology and distribution was also observed in the samples that were annealed under the -30DP and $+5\text{DP}$ process atmospheres (Figures 4 and 5), where, under the same processing conditions, a finer and more globular surface oxide structure can be clearly observed for the Sn-added substrates as opposed to the coarse and more film-like oxide layers of the reference steel. Furthermore, in terms of oxide distribution, a wider spacing between the oxides as well as less surface oxide coverage could be identified for the Sn-added samples.

As mentioned earlier, the effect of the process atmosphere oxygen potential—adjusted using the process atmosphere dew point—on the selective oxidation of the alloying elements was also determined. Comparison of the micrographs in Figures 3, 4, and 5 showed that, as a general trend, the isochronal oxide surface coverage decreased by increasing the process atmosphere dew point from 223 K to 278 K ($-50\text{ }^\circ\text{C}$ to $+5\text{ }^\circ\text{C}$), such that the maximum surface coverage was obtained for the samples annealed under the -50DP process atmosphere. Additionally, the oxides formed under the -50DP and -30DP process atmospheres were, overall, more closely spaced, forming continuous surface films, compared to those of the $+5\text{DP}$ atmosphere which exhibited a more discrete, nodule-like morphology (Figures 3 and 4 vs 5). This trend was consistent for both of the experimental steels.

Mn and Si (inset) XPS depth profiles of the experimental steels for the 120 and 600 seconds intercritical annealing times as a function of process atmosphere dew point are given in Figure 6, where the dashed line and open data points represent the elemental profiles of the Sn-added steel. It should be mentioned that, for the sake of avoiding congestion in the plot, only the 120- and 600-second data are shown; however, the results of 360-second hold were intermediate to the two. XPS binding energy data from the 120-second samples for each process atmosphere examined were used to determine the chemical state of the surface oxides. Binding energies of 530.3, 641.4, and 654.1 eV were determined for the O1s, $\text{Mn}2p_{3/2}$, and $\text{Mn}2p_{1/2}$ peaks, respectively, which correspond to those reported for MnO by several authors.^[38–40] It should be noted, however, that the Si signals were too noisy to provide reliable interpretation of the binding energy data.

It can be inferred from Figure 6(a) that the thickness of the external MnO for both steels increased with increasing annealing time for the -50DP samples, where the external MnO layer was significantly thicker for the reference steel for the annealing time of 600 seconds. These observations are qualitatively in agreement with the SEM observations of external oxide coarsening shown in Figure 3. However, in the case of the 120-second samples, the thicknesses of the MnO layers were comparable. Furthermore, all plots in Figure 6(a) converged to the bulk Mn content at

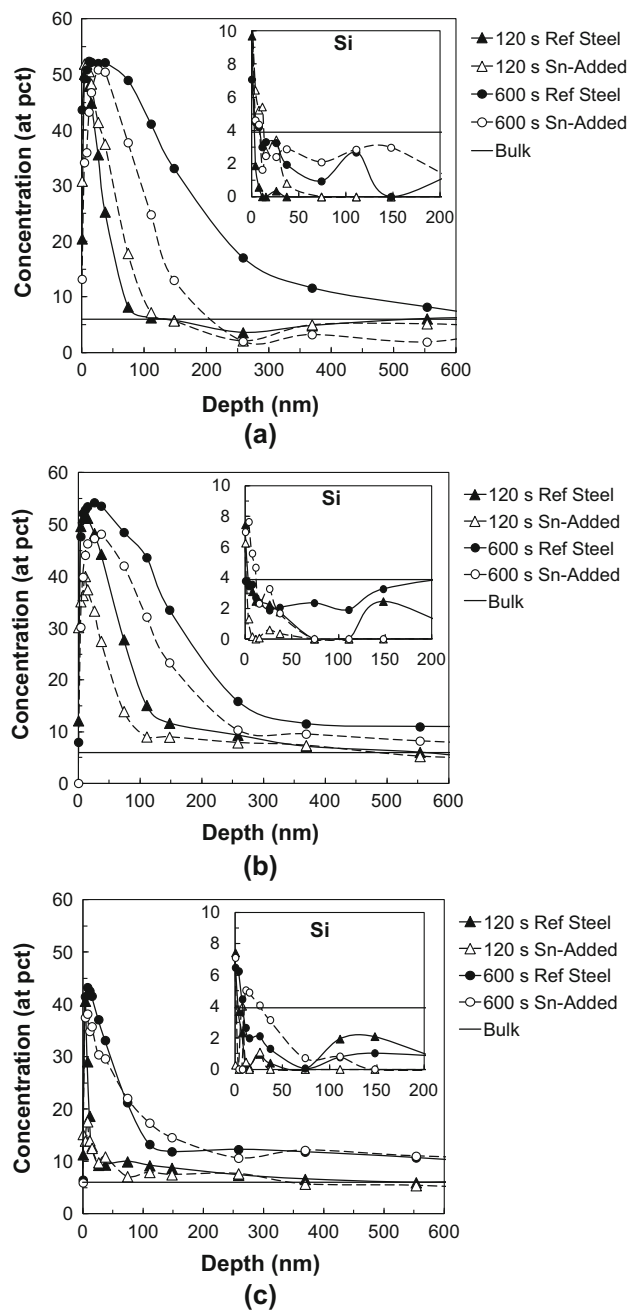


Fig. 6—XPS depth profiles of Mn and Si (inset) of the reference and Sn-added steels annealed for 120 and 600 s under the (a) -50DP , (b) -30DP , and (c) $+5\text{DP}$ process atmospheres.

approximately 200 nm with the exception of the reference steel annealed for 600 seconds, which returned to the bulk value at approximately 600 nm. No significant enrichment of Si was detected, aside from a slight increase observed at the outmost surface layer of the steels.

The XPS elemental profiles acquired from the -30DP samples in Figure 6(b) showed the same trend with increasing annealing time as was shown in the SEM observations in Figure 4 *i.e.*, the thickness of the external oxide layer tended to increase with increasing

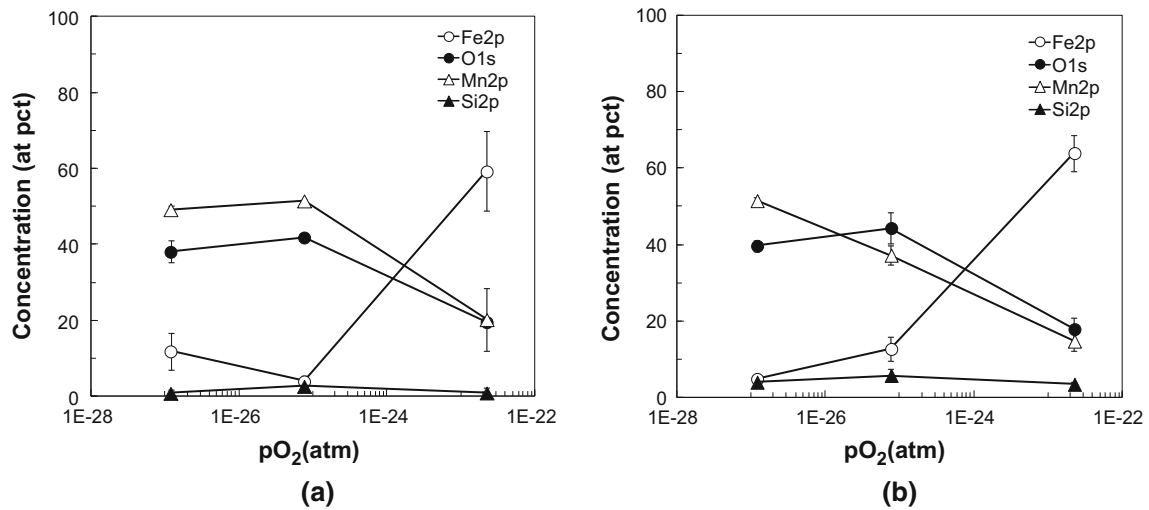


Fig. 7—XPS chemical composition from the top 20 nm of the external oxide layer on the (a) reference steel and (b) Sn-added steels annealed for 120 s as a function of process atmosphere oxygen partial pressure.

annealing time. Furthermore, a decrease in the surface Mn enrichment relative to the reference alloy was detected in the case of the Sn-added substrates for a given annealing time, implying that the external oxide was somewhat thinner. It is also worth noting that, under the $-30DP$ process atmosphere, the 600-second Mn profiles of both grades maintained larger values than the bulk concentration to further depths from the surface relative to the observations for the $-50DP$ samples annealed for the same time. Also, similar to the $-50DP$ depth profile observations, only a minimal enrichment of Si was detected at the surface.

A significant decrease in the external MnO layer thickness was observed in the XPS plots of the $+5DP$ process atmosphere samples compared to the other process atmospheres, as can be seen in Figure 6(c), in agreement with the trends from the SEM analysis (Figures 3 through 5). All elemental profiles of the $+5DP$ process atmosphere samples presented evidence of internal oxidation having taken place as values above 6 at. pct were detected further away from the surface, consistent with the external to internal oxidation transition having taken place when annealing under higher pO_2 process atmospheres (Table II). However, as can be seen from the inset in Figure 6(c), the slight enrichment of Si was, again, confined only to the surface of the samples.

Figures 7(a) and (b) show the variation in chemical composition of the external oxides formed during the 120-second anneal vs the process atmosphere pO_2 . The elemental concentrations in these plots were averaged from the top 20 nm of the surface after a 5 nm sputter to remove any surface contamination, where the error bars represent the sample standard deviation. It can be seen that, for both steel chemistries, the amount of metallic iron (Fe2p peak) at the steel surface increased with increasing process atmosphere oxygen partial pressure and coincided with a decrease in the O and Mn concentrations. It is worth noting that the Mn to O ratios remained relatively constant at approximately one

under all experimental conditions, consistent with the binding energy determination that the external oxides were MnO. The amount of metallic iron was also found to be comparable between the two alloys for all process atmospheres.

Using the FIB-derived cross-sectional images of the surface and subsurface (Figure 2), the effect of process atmosphere pO_2 and alloy Sn addition on the external and internal oxide growth kinetics were determined, the results of which are plotted in Figures 8(a) and (b) for the external oxide thickness and depth of the internal oxidation zone vs the square root of time, respectively. Given the significant local variation in the thickness of the oxide layers/zones, the average of a minimum of 100 measurements are reported, where the error bars represent the 95 pct confidence interval of the mean. It should be mentioned that the coefficient of determination (*i.e.*, R^2 value) of all of the regression lines was above 0.96, with the exception of the $-50DP$ and $-30DP$ lines for the internal oxidation of the Sn-added steel, which were 0.91. This near-perfect linear fit is indicative of parabolic growth rate kinetics under all experimental conditions, which would be expected for the case of diffusion-controlled oxidation.^[41] However, the most notable result from these plots is the decreased oxide growth kinetics for the Sn-containing steels compared to the reference alloy. It can be inferred from the line slopes in Figure 8(a) that the growth rate of the external oxides was highest for the reference steel annealed under the $-30DP$ atmosphere, followed by that of the Sn-containing grade for the same process atmosphere. The external oxide growth rates for the remaining process atmospheres and alloys fell below those of the above two with the rates being comparable.

The effect of alloy Sn addition on the oxidation rate was more pronounced when examining the internal oxidation kinetics data shown in Figure 8(b), where a clear decrease in growth rate can be identified for the Sn-added steels. The maximum depth of internal oxidation and the maximum internal oxidation growth rate was observed

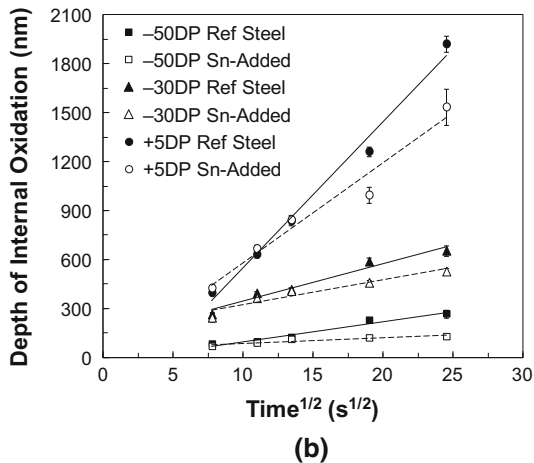
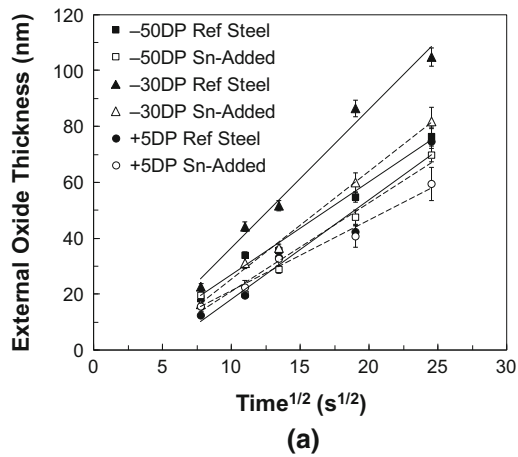


Fig. 8—Growth kinetics of (a) external oxide thickness and (b) depth of internal oxidation zone as a function of process atmosphere dew point and Sn addition.

for the reference steel annealed under the + 5DP atmosphere, followed by the Sn-added steels annealed under this process atmosphere (2 vs 1.5 μm for the 600-second holds, respectively). Annealing under the - 30DP and - 50DP atmospheres resulted in a significant decrease in the internal oxidation rates in comparison with the + 5DP process atmosphere, with the Sn-containing steels exhibiting significantly slower growth kinetics vs those of the reference alloy. The suppression of external and internal oxidation kinetics by large metallic atom additions to steels has been previously observed and reported in the works of Lyudkovsky,^[19] Zhang *et al.*,^[23] and Cho *et al.*,^[20–22] where the operative mechanism was determined to be segregation of the high atomic number alloying elements to the surface—in the present case, Sn—occupying the surface oxygen adsorption sites, thereby reducing the concentration of dissolved oxygen at the surface and the inward oxygen flux.

HR-STEM analysis of both the reference and Sn-added alloys annealed for 600 seconds under the - 50DP, - 30DP, and + 5DP process atmospheres were performed on the FIB cross-sections, where the corresponding images are provided in Figures 9(a) through (f). The black area at the top of these images is the C that was deposited prior to FIB milling to

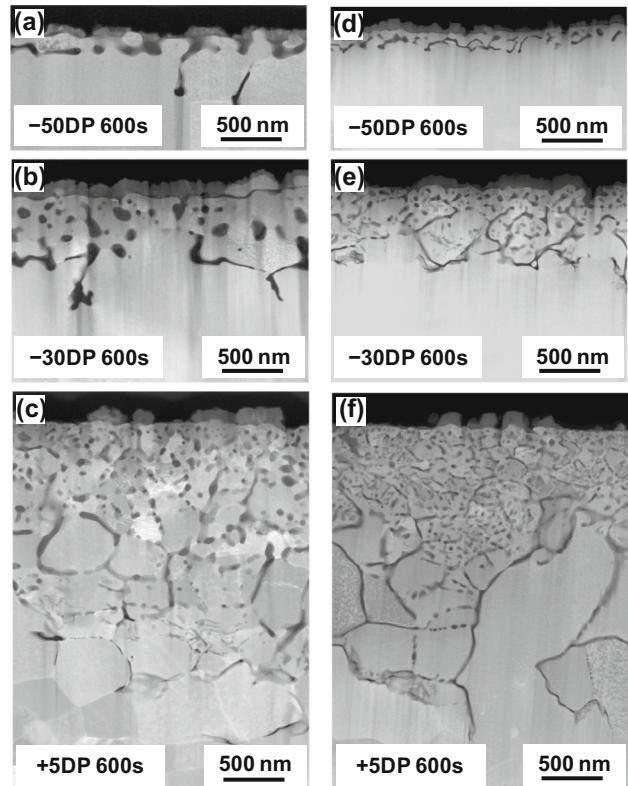


Fig. 9—Dark field STEM images from cross-sections of (a) through (c) the reference steel and (d) through (f) the Sn-added steel annealed for 600 s under the - 50DP, - 30DP, and + 5DP process atmospheres, respectively.

protect the external oxides from damage. It should be noted that samples taken from shorter annealing times displayed the same morphological trends documented above, with the 600 seconds annealing time samples being chosen here for increased clarity. The refinement effect of the Sn addition on the oxide morphology and distribution of the external and internal oxide network is clearly observed in these images. Consistent with the SEM observations in Figures 3(c) and 4(c), it can be seen from Figures 9(a) and (b) that the reference alloy external oxides under the - 50DP and - 30DP process atmospheres formed continuous films. In contrast to this, the Sn-added samples annealed under the same process atmospheres (Figures 9(d) and (e)) showed a significantly thinner and discontinuous surface oxide morphology. It can also be observed that the depth of the internal oxidation zone had slightly decreased in the case of the Sn-containing substrates, consistent with the observations in Figure 8. The external oxide morphology for both steels when annealed under the + 5DP atmosphere was found to be nodule-like as opposed to film-like; however, the external oxide structures for the Sn-added alloy shown in Figure 9(f) showed a globular, more widely spaced morphology. Finally, it can be observed that the depth of internal oxidation increased when higher process atmosphere $p\text{O}_2$ were employed, which was expected due to the increased oxygen flux shifting the oxidation mode strongly to the internal oxidation mode, as was previously shown in Figure 8.

The TEM cross-sections were also analyzed by EELS to determine the chemistry of the external and internal oxides observed in the alloys. An example of such an analysis is shown in Figure 10(a) where Fe, O, Mn, and Si elemental maps were extracted from the EELS spectra acquired from the reference steel annealed for 600 seconds under the -50DP process atmosphere. In accordance with the XPS findings, it can be seen from these maps that the surface oxides were largely composed of Mn and O, where no significant Si signal was detected in the surface nodules. However, a thin layer of Si enrichment was found at the oxide/steel interface, which correlates with the subtle Si enrichment detected in the Si XPS depth profiles of Figure 6(a). Furthermore, the continuous internal oxides showed a varying composition. As marked by arrows in the Mn and Si maps, in some areas the internal oxides were significantly enriched in Si and O with no Mn enrichment and in other regions Mn, Si, and O were present, suggesting a Mn-Si oxide chemistry. In order to identify the oxide species present, the O-K, Mn-L_{2,3}, and Si-K edges of the acquired EELS spectra were compared with those of the standards available in the literature.^[42–48] The high-resolution EELS spectra are shown in Figure 10(b), where the core-loss peaks and the near-edge fine structures that allowed for speciation of the oxides are marked by vertical arrows. The O-K and Mn-L_{2,3} peaks of the spectra acquired from the external oxides correlated with those of MnO,^[42–45] consistent with the binding energy determination from XPS (Figures 6 and 7). In the case of the internal oxides that were Mn-rich, shown by the blue line in Figure 10(b), the O-K core-loss and Mn-L_{2,3} near-edge features agreed with those determined for MnSiO₃ by Grosvenor *et al.*,^[46] where the presence of the Si edge in the high-loss energy window confirmed that a manganese silicate was present in those regions. Similarly, the internal oxides that were enriched

in Si only were identified as SiO₂.^[47,48] Similar TEM and EELS analyses were carried out for all of the samples shown in Figure 9 and showed the same trends as those presented above—*i.e.*, the external oxides were consistently identified as MnO while the internal oxide networks comprised a multi-layered structure with MnSiO₃ surrounding a SiO₂ core for both the bulk internal and grain boundary oxides.

Given the extremely low bulk concentration of Sn (*i.e.*, 0.05 wt pct or 0.02 at. pct) and as no evidence of Sn segregation could be found with either XPS or EELS, 3D APT analysis of the steel/external oxide interface was conducted on a specimen taken from a $-30\text{DP} \times 600\text{-second}$ Sn-added sample in order to locate and quantify any Sn segregation at the atomic scale. The results of this analysis are presented in Figure 11, where the Fe, Mn, and Si atom maps of the reconstructed volume across the external MnO/steel interface are shown in Figure 11(a). The color composition map taken from a 5-nm-thick slice of the reconstructed external oxide/substrate interface is shown in Figure 11(b). It should be pointed that the Sn signal was too weak to be properly visualized in this map; however, in accordance with the TEM + EELS observations (Figure 10(a)), the Si-rich layer underneath the external MnO oxide was observed at the substrate interface.

Elemental concentration profiles across the oxide/substrate interface are shown in Figure 11(c), with the Sn profile magnified in a separate plot underneath. From this, it can be inferred that Sn was segregated to the steel/oxide interface with an enrichment level approximately ten times that of the bulk concentration—*i.e.*, 0.02 at. pct. It should be mentioned that, aside from the Si and Sn enrichments at this interface, the elemental concentration profiles also show a layer rich in Fe and O which is at odds with the previous analysis and is also

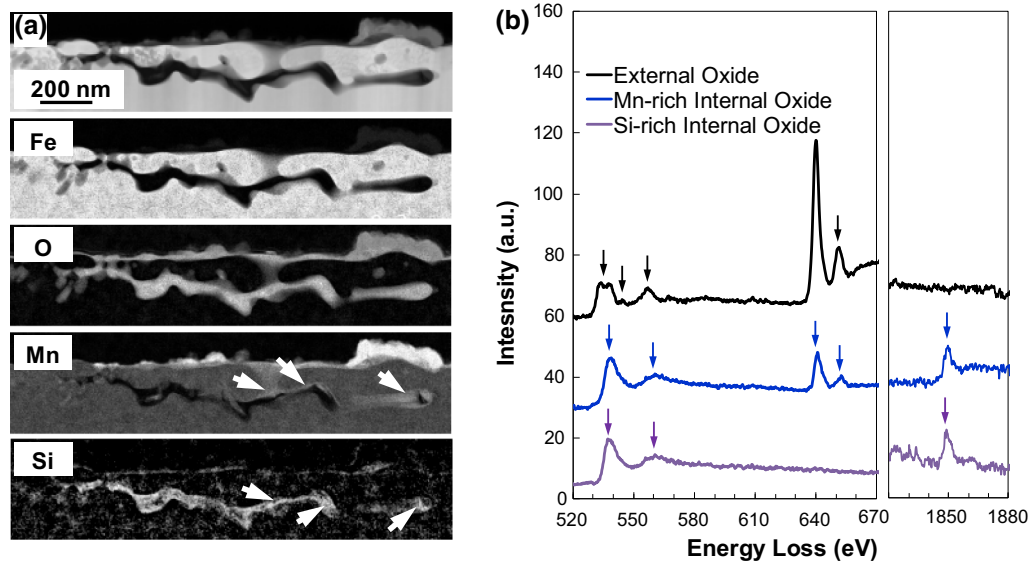


Fig. 10—(a) Dark field STEM image and EELS elemental maps of the surface and subsurface oxides formed in the reference steel annealed for 600 s under the -50DP atmosphere and (b) the corresponding electron energy loss spectra showing the fine structures of the O-K, Mn-L_{2,3}, and Si-K edges (Color figure online).

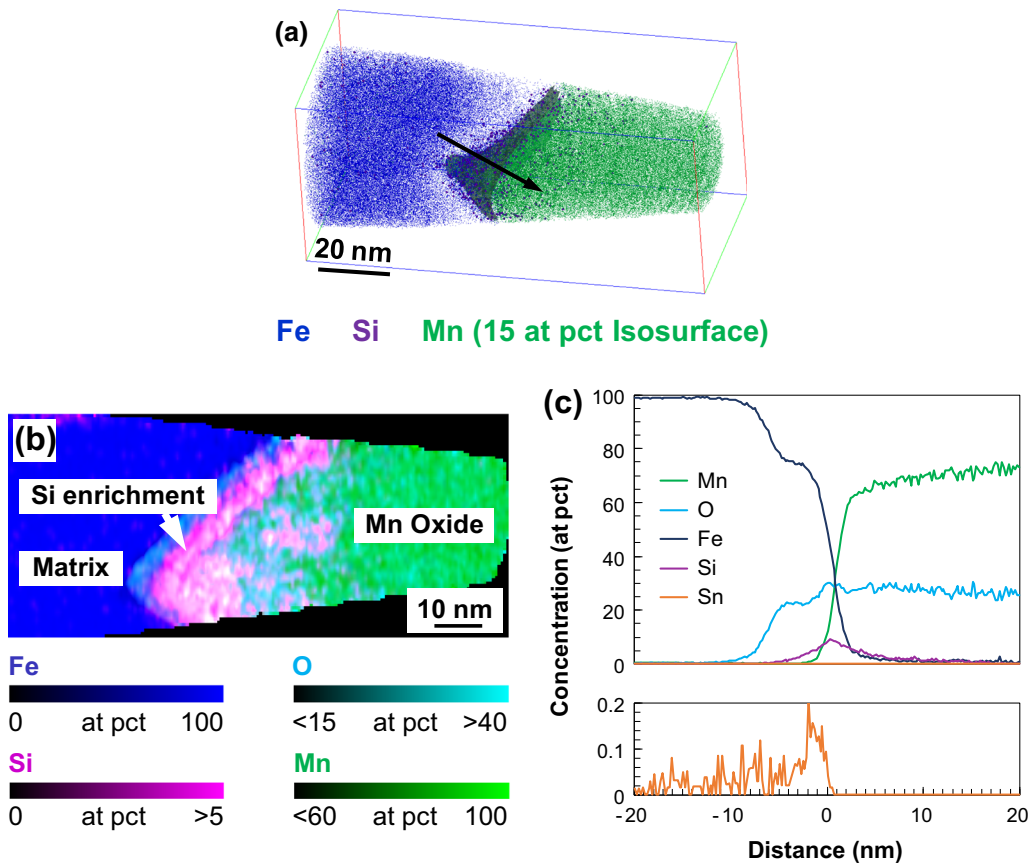


Fig. 11—APT analysis of the external oxide/substrate interface of the Sn-added steel annealed for 600 s under the -30DP atmosphere (a) 3D atom map of Fe, Mn, Si, and 15 at. pct Mn isosurface, (b) 5-nm-thick 2D section of the reconstructed needle showing the enrichment of alloying elements in the surface oxide, and (c) proximity histogram (proxigram) revealing the 1D concentration profiles normal to the isosurface marked with an arrow in (a) (Color figure online).

unexpected given the fact that all process atmospheres in the present study were fully reducing with respect to Fe. This effect is a known artifact of APT analysis, in which O is preferentially retained when the analysis direction runs from an oxide into a metal.^[49] Additionally, the Mn to O ratio of the surface oxide was found to be higher than that of MnO which can to some extent be attributed to oxygen loss during field evaporation.

IV. DISCUSSION

It was consistently determined through several analytical microscopy techniques that significant changes to the oxide morphology, distribution, and thickness resulted from adding 0.05 wt pct Sn to the model 6Mn-2Si steel (Figures 3 through 9). The external MnO oxides formed on the surface of the Sn-containing steels exhibited a more widely spaced distribution of fine, globular nodules (Figures 3 through 5(d) through (f)) vs their non-Sn-added counterparts, which displayed a significantly more compact, coarser external oxide morphology (Figures 3 through 5(a) through (c)). This change in external oxide morphology was also accompanied by slower external oxidation kinetics (Figure 8(a)) resulting in thinner external MnO layers

on the Sn-added alloys compared to those of the reference steels (Figure 6(a)). Strong oxide refinement and slower oxidation kinetics were similarly observed in the case of the internal oxidation, as pictured in Figures 8(b) and 9, where the internal oxidation rates were uniformly lower for the Sn grade vs the reference steel for all process atmospheres.

On the other hand, the external oxide chemistry was not found to be affected by the 0.05 wt pct Sn addition. As can be seen from the plots in Figure 7, an approximate 1:1 ratio of Mn to O for the external oxides was maintained for all experimental conditions, which, in combination with the XPS binding energy data and the EELS analysis (Figure 10) determined the external oxides to be MnO for both steel compositions. Similarly, EELS analysis (Figure 10) showed that the internal oxides comprised a layered structure with the oxide cores and the surrounding shells being identified as SiO_2 and MnSiO_3 , respectively.

The formation mechanism of the observed oxide species, which all formed thermodynamically stable oxides under the process atmospheres of this study, can be explained by the kinetic and thermodynamic factors in play. SiO_2 was first formed at the grain boundaries of the subsurface, owing to its higher thermodynamic stability,^[50,51] near-zero solubility product^[52] compared

to that of MnO, and the higher diffusivity of Si relative to Mn.^[53] Due to the slower diffusion of Mn to the reaction sites and its higher thermodynamic stability and lower solubility vs MnO,^[52] MnSiO₃ was formed at the outer surfaces of the grain boundary SiO₂, *i.e.*, the oxide shells (Figure 10). The presence of the thin external MnSiO₃ layer (Figure 10) can also be described by the same reaction sequence. At the surface, under a continuous supply of oxygen from the process atmosphere and the lack of competition among Si and Mn for the dissolved oxygen consumption, the higher solubility MnO formed stable oxides as a locally high Mn to Si ratio was also present. The presence of MnO as the surface oxide species has been reported in several previous works^[50,54,55] and more recently in the case of the medium-Mn 3G steels, by Pourmajidian and McDermid.^[56,57]

The selective oxidation of Mn and Si was also affected by the process atmosphere oxygen partial pressure. The external MnO oxides observed on the surface of the reference steel annealed under the – 50DP and – 30DP process atmospheres (Figures 3 and 4(a) through (c)) comprised a patchy and film-like morphology with large fractions of the substrate surface being covered by these structures. It should be noted that, in the case of the Sn-added substrates, a finer globular morphology with thin films between the nodules was observed in Figures 3 and 4(d) through (f), despite the external oxidation mode being dominant, particularly under the – 50DP atmosphere. Furthermore, the accelerated external oxidation kinetics observed under the – 30DP process atmosphere (Figure 8(a)) can be explained by the higher oxygen potential of this process atmosphere (Table II) compared to the – 50DP atmosphere, and by the fact that the – 30DP process atmosphere pO₂ is close to the external-internal transition pH₂O/pH₂ at the IAT of 963 K per Wagner model^[58] calculations. Annealing under the + 5DP atmosphere resulted in a significantly thinner external MnO layer (Figures 5, 6(c) and 8). However, the higher pO₂ of this atmosphere (Table II) led to a stronger internal oxidation mode, as characterized by the increased depth of the internal oxidation zone under the + 5DP process atmosphere, per the kinetic data in Figure 8(b) and the cross-sectional TEM images in Figure 9. This shift in the oxidation mode also resulted in significantly more metallic Fe being available within 20 nm of the surface (Figure 7), which further implies the presence of very thin MnO nodules in these structures. Both of these factors would very likely have significant benefits in the subsequent reactive wetting with the continuous galvanizing bath.

Given the above relatively uniform results on the effect of the Sn addition on the oxidation kinetics, it can be concluded that the interfacial Sn segregation layer—as detected by 3D APT (Figure 11)—was responsible for reducing the observed oxidation rates and for modifying the distribution and morphology of both the external and internal oxides. Previous authors have stated that, as a result of interfacial segregation of the surface active elements in low-alloy TRIP steels, the interfacial energies can change such that formation of surface oxides with lens-type morphology is encouraged

as opposed to film-type growth.^[21,22] The effect of surface active elements such as Sb, Sn, and Bi on the retardation of internal oxidation kinetics has also been previously reported in both low-alloy TRIP steels and Si-containing electrical steels.^[19–25] The large atomic size mismatch between such elements and Fe acts as a driving force for segregation of these elements to the free surfaces or interfaces in order to reduce the elastic strain energy of the bulk lattice.^[25,26] For example, Lyudkovsky^[19] reported that the addition of 0.08 wt pct Sb to Si-Al electrical steels significantly reduced the rate of internal oxidation in a high pO₂ N₂-H₂ gas mixture due to the segregation of Sb to the grain boundaries reducing the inward diffusion of oxygen by blocking the short-circuit diffusion paths. This effect of Sb on suppressing the depth of internal oxidation was also reported^[23,24] in the case of IF and TRIP steel substrates and was explained by showing that enrichment of Sb to the surface occupied the surface O adsorption sites, thereby decreasing the oxygen permeability of the surface.

More recently, the effects of Sn additions within the range of 0.05 wt pct to 1 wt pct^[21] and Bi additions of 0.05 to 0.2 wt pct^[22] on the selective oxidation of 0.1C-1.6Mn-1.5Si TRIP substrates were investigated. It was reported that the addition of 0.05 wt pct Sn affected both the external and internal oxidation such that a decrease in the depth of internal oxidation and a change in morphology of the Si-rich surface oxides were observed, while no change in the Mn-rich oxides was detected. Furthermore, it was found that the chemistry of the surface oxides was also altered due to the reduced oxygen solubility at the surface such that the Mn to Si ratio of the oxides decreased with increasing Sn contents.^[21]

In the present work, however, the 0.05 wt pct addition of Sn to the medium-Mn 3G-AHSS system did not change the surface oxide chemistry and MnO was found to be the only oxide species present at the external surface of all samples. This is due to the fact that, unlike the above-mentioned study,^[21] the Sn addition was kept to a minimum and, furthermore, the significantly higher Mn to Si ratio in the present alloy promoted MnO formation rather than Mn-Si oxides.^[50,54–57] It was also previously reported that only the morphology of the Si-rich manganese silicates were affected as a result of the Sn addition, with the exception of the case of excessive Sn addition (1 wt pct), where the granular morphology of the MnO oxides was changed to a lens-type.^[21] Nevertheless, significant morphological changes of the nodular surface MnO as well as suppression of the oxidation kinetics took place in the present 0.1C-6Mn-2Si steel as a result of the 0.05 wt pct Sn addition.

It has been shown by several authors^[9–12,35,59,60] that successful reactive wetting by the continuous galvanizing Zn(Al,Fe) bath is attainable despite external selective oxidation if the oxide morphology exhibits a widely spaced, nodular morphology with relatively thin oxide films between the nodules or for an overall thin external oxide. While it is well known that film-forming Si-rich surface oxides are detrimental to reactive wetting and

integral Fe-Al interfacial layer formation, it should also be noted that previous studies^[32,34,59] have shown that, even in the case of surfaces covered exclusively with MnO, successful reactive wetting can be obtained only when the surface MnO is thin enough for aluminothermic reduction to take place during industrially relevant immersion times in a 0.20 wt pct Al (dissolved) galvanizing bath, *i.e.*, surface film thicknesses under 85 nm.^[34]

Significant improvement in the galvanized coating quality of a 0.1C-1.5Si-1.6 Mn TRIP steel was obtained as a result of a 0.05 wt pct Sn addition and the consequent morphological change of the Si-rich surface oxides.^[20,21] For the alloy system and the process atmospheres of the present study, it was found that MnO was the dominant external oxide phase while Si was enriched at the surface oxide/steel interface and, more predominantly, in the subsurface. A variety of surface oxide morphologies, thicknesses, and distributions were observed under each combination of experimental alloy and process atmosphere pO₂. It was found that the most desirable external oxide morphology with respect to promoting reactive wetting was formed under the combined use of the 0.05 wt pct Sn addition and high process atmosphere oxygen partial pressures. It is, therefore, expected that the Sn-containing substrates, particularly those annealed under the -30DP and +5DP process atmospheres, would exhibit significantly improved reactive wetting by the continuous galvanizing bath due to the widely spaced distribution of significantly thinner and finer globular surface MnO compared to those of the reference steel, as these type of surface oxide structures can promote Fe dissolution into the Zn(Al,Fe) galvanizing bath leading to the formation of the desirable Fe₂Al₅Zn_x interfacial layer during immersion.

V. CONCLUSIONS

The selective oxidation of a 0.1C-6Mn-2Si medium-Mn steel as functions of process atmosphere oxygen partial pressure, annealing time, and a 0.05 wt pct Sn addition was investigated using CGL-compatible intercritical annealing heat treatments.

Adding 0.05 wt pct Sn to the steel chemistry modified the morphology and distribution of the external MnO oxides from a continuous film-like layer to a finer and discrete globular morphology under all experimental process atmospheres. The bulk internal oxidation region and grain boundary oxide networks formed in the Sn-containing steel were also significantly refined compared to those observed for the reference alloy. A decrease in external MnO thickness, accompanied with an increase in the amount of metallic iron available, was determined with increasing process atmosphere oxygen partial pressure, where smaller area fractions of the steel surface were covered by thick MnO oxides.

External and internal oxidation kinetic rate data determined that both external and internal oxidation rates were suppressed as a result of the Sn addition by reducing the oxygen solubility at the surface. The

thickest external oxide layer was observed in the reference steels annealed under the 243 K (-30 °C) dew-point atmosphere and the thinnest surface layer belonged to that of the Sn-added grade annealed under 278 K (+5 °C) dew-point. In contrast, the maximum depth of internal oxidation was observed for the samples annealed under the 278 K (+5 °C) dew-point process atmosphere.

Significant segregation of Sn at the oxide/metal interface was detected by 3D atom probe tomography, which was approximately ten times that of the bulk concentration. This segregation was likely responsible for the observed refinement of the external/internal oxides and the retardation effects on the oxidation reaction kinetics.

The reactive wetting of the present medium-Mn 3G model alloy by the continuous galvanizing zinc bath is expected to be significantly improved, given the positive morphological changes of the external MnO, due to alloying the 0.1C-6Mn-2Si steel with a trace amount (0.05 wt pct) of Sn.

ACKNOWLEDGMENTS

This work was financially supported by the Natural Sciences and Engineering Research Council of Canada (NSERC) and Stelco Inc. through the NSERC/Stelco Industrial Research Chair in Advanced Coated Steels (Grant IRCPJ 305921-12). U.S. Steel Research is gratefully acknowledged for their provision of the steels used in this study. The authors would like to thank John Thomson and Ray Fullerton of the McMaster Steel Research Centre for their technical support with the galvanizing simulations, Travis Casagrande and Dr. Andreas Korinek of the Canadian Centre for Electron Microscopy (CCEM) for technical and scientific assistance with FIB work and electron energy loss spectroscopy, and Dr. Li Sun at ArcelorMittal Dofasco for aiding with the XPS analyses.

REFERENCES

1. D.W. Suh and S.J. Kim: *Scripta Mater.*, 2017, vol. 126, pp. 63–67.
2. M.J. Merwin: *Mater. Sci. Forum*, 2007, vol. 539, pp. 4327–32.
3. M.J. Merwin: *Iron Steel Technol.*, 2008, vol. 5, pp. 66–84.
4. R.L. Miller: *Metall. Mater. Trans. B*, 1972, vol. 3B, pp. 905–12.
5. K.M.H. Bhadhon, J.R. McDermid, and F.E. Goodwin: *The 10th International Conference on Zinc and Zinc Alloy Coated Steel Sheet (Galvatech 2015)*, 2015, pp. 936–43.
6. J. Mahieu, S. Claessens, and B.C. De Cooman: *Metall. Mater. Trans. A*, 2001, vol. 32A, pp. 2905–08.
7. J. Mahieu, B.C. De Cooman, and S. Claessens: *Mater. Sci. Technol.*, 2003, vol. 19, pp. 125–31.
8. J. Mahieu, B.C. De Cooman, J. Maki, and S. Claessens: *Iron Steelmak.*, 2002, vol. 29, pp. 29–34.
9. E.M. Bellhouse and J.R. McDermid: *Metall. Mater. Trans. A*, 2011, vol. 42A, pp. 2753–68.
10. E.M. Bellhouse and J.R. McDermid: *Metall. Mater. Trans. A*, 2012, vol. 43A, pp. 2426–41.
11. E.M. Bellhouse and J.R. McDermid: *Metall. Mater. Trans. A*, 2010, vol. 41A, pp. 1539–53.

12. L. Cho, S.J. Lee, M.S. Kim, Y.H. Kim, and B.C. De Cooman: *Metall. Mater. Trans. A*, 2013, vol. 44A, pp. 362–71.
13. Y.F. Gong, H.S. Kim, and B.C. De Cooman: *ISIJ Int.*, 2009, vol. 49, pp. 557–63.
14. Y.F. Gong, H.S. Kim, and B.C. De Cooman: *ISIJ Int.*, 2008, vol. 48, pp. 1745–51.
15. K.R. Jo, L. Cho, J.H. Oh, M.S. Kim, K.C. Kang, and B.C. De Cooman: *Metall. Mater. Trans. A*, 2017, vol. 48A, pp. 3635–41.
16. M. Blumenau, M. Norden, F. Friedel, and K. Peters: *Surf. Coat. Technol.*, 2011, vol. 206, pp. 559–67.
17. Y.F. Gong and B.C. De Cooman: *ISIJ Int.*, 2011, vol. 51, pp. 630–37.
18. A. Ruck, D. Monceau, and H.J. Grabke: *Steel Res.*, 1996, vol. 67, pp. 240–46.
19. G. Lyudkovsky: *IEEE Trans. Magn.*, 1986, vol. 22, pp. 508–46.
20. L. Cho, M.S. Kim, Y.H. Kim, and B.C. De Cooman: *Metall. Mater. Trans. A*, 2014, vol. 45A, pp. 4484–98.
21. L. Cho, E.J. Seo, G.S. Jung, D.W. Suh, and B.C. De Cooman: *Metall. Mater. Trans. A*, 2016, vol. 47A, pp. 1705–19.
22. J. Oh, L. Cho, M. Kim, K. Kang, and B.C. De Cooman: *Metall. Mater. Trans. A*, 2016, vol. 47A, pp. 5474–86.
23. Z.T. Zhang, I.R. Sohn, F.S. Pettit, G.H. Meier, and S. Sridhar: *Metall. Mater. Trans. B*, 2009, vol. 40B, pp. 567–84.
24. Y.Y. Zhang, Y.Y. Zhang, F.H. Yang, and Z.T. Zhang: *J. Iron. Steel Res. Int.*, 2013, vol. 20, pp. 39–56.
25. E.D. Hondores and M.P. Seah: *Int. Met. Rev.*, 1977, vol. 22, pp. 262–301.
26. M. Seah: *J. Catal.*, 1979, vol. 57, pp. 450–57.
27. D. Melford: *Philos. Trans. R. Soc. A*, 1980, vol. 295, pp. 89–103.
28. D.K. Matlock, J.G. Speer, E. De Moor, and P.J. Gibbs: *JES-TECH*, 2012, vol. 15, pp. 1–12.
29. B.C. De Cooman, P. Gibbs, S. Lee, and D.K. Matlock: *Metall. Mater. Trans. A*, 2015, vol. 44A, pp. 2563–72.
30. S. Lee, K. Lee, and B.C. De Cooman: *Metall. Mater. Trans. A*, 2013, vol. 46A, pp. 2356–63.
31. S. Lee and B.C. De Cooman: *Metall. Mater. Trans. A*, 2013, vol. 45A, pp. 709–16.
32. R. Khondker, A. Mertens, and J.R. McDermid: *Mater. Sci. Eng. A*, 2007, vol. 463, pp. 157–65.
33. E.M. Bellhouse and J.R. McDermid: *Mater. Sci. Eng. A*, 2008, vol. 491, pp. 39–46.
34. R. Kavitha and J.R. McDermid: *Surf. Coat. Technol.*, 2012, vol. 212, pp. 152–58.
35. R. Sagl, A. Jarosik, D. Stifter, and G. Angeli: *Corros. Sci.*, 2013, vol. 70, pp. 268–75.
36. Morris: *FREED Thermodynamic Database*, v7.8.1, 2013.
37. K. Thompson, D. Lawrence, D.J. Larson, J.D. Olson, T.F. Kelly, and B. Gorman: *Ultramicroscopy*, 2007, vol. 107, pp. 131–39.
38. B.R. Strohmeier and D.M. Hercules: *J. Phys. Chem.*, 1984, vol. 88, pp. 4922–29.
39. M.C. Biesinger, B.P. Payne, A.P. Grosvenor, L.W.M. Lau, A.R. Gerson, and R. St.C. Smart: *Appl. Surf. Sci.*, 2011, vol. 257, pp. 2717–30.
40. A. Aoki: *Jpn. J. Appl. Phys.*, 1976, vol. 15, pp. 305–11.
41. N. Birks, G.H. Meier, and F.S. Pettit: *Introduction to the High-Temperature Oxidation of Metals*, 2nd ed., Cambridge University Press, Cambridge, 2006, p. 338.
42. J.H. Rask, B.A. Miner, and P.R. Buseck: *Ultramicroscopy*, 1987, vol. 21, pp. 321–26.
43. P.L. Potapov, K. Jorissen, and D. Schryvers: *Phys. Rev. B*, 2004, vol. 70, pp. 1–10.
44. H.K. Schmid and W. Mader: *Micron*, 2006, vol. 37, pp. 426–32.
45. H. Tan, J. Verbeeck, A. Abakumov, and G. Van Tendeloo: *Ultramicroscopy*, 2012, vol. 116, pp. 24–33.
46. A.P. Grosvenor, E.M. Bellhouse, A. Korinek, M. Bugnet, and J.R. McDermid: *Appl. Surf. Sci.*, 2016, vol. 379, pp. 242–48.
47. K. Kimoto, T. Sekiguchi, and T. Aoyama: *J. Electron Microsc.*, 1997, vol. 46, pp. 369–74.
48. Gatan, <http://www.eels.info/atlas/silicon>. Accessed 12 June 2017.
49. E.A. Marquis, B.P. Geiser, T.J. Prosa, and D.J. Larson: *J. Microsc.*, 2011, vol. 24, pp. 225–33.
50. X.S. Li, S.I. Baek, C.S. Oh, S.J. Kim, and Y.W. Kim: *Scripta Mater.*, 2007, vol. 57, pp. 113–16.
51. Y. Suzuki, T. Yamashita, Y. Sugimoto, S. Fujita, and S. Yamaguchi: *ISIJ Int.*, 2009, vol. 49, pp. 564–73.
52. D. Huin, P. Flauder, and J.B. Leblond: *Oxid. Met.*, 2005, vol. 64, pp. 131–67.
53. J. Takada, K. Kashiwagi, and M. Adachi: *J. Mater. Sci.*, 1984, vol. 19, pp. 3451–58.
54. H. Liu, W. Shi, Y. He, and L. Li: *Surf. Interface Anal.*, 2010, vol. 42, pp. 1685–89.
55. M. Auinger, V.G. Praig, B. Linder, and H. Danninger: *Corros. Sci.*, 2015, vol. 96, pp. 133–43.
56. M. Pourmajidian and J.R. McDermid: *Mater. Met. Trans. A*, 2018, vol. 49A, pp. 1795–1808.
57. M. Pourmajidian and J.R. McDermid: *ISIJ Int.*, 2018, <https://doi.org/10.2355/isijinternational.ISIJINT-2017-688>.
58. C. Wagner: *Zh. Elektrochem.*, 1959, vol. 63, pp. 772–82.
59. S. Alibeigi, R. Kavitha, R.J. Meguerian, and J.R. McDermid: *Acta Mater.*, 2011, vol. 59, pp. 3537–49.
60. R. Sagl, A. Jarosik, G. Angeli, T. Haunschmid, G. Hesser, and D. Stifter: *Acta Mater.*, 2014, vol. 72, pp. 192–99.